This article has been accepted for publication in IEEE Robotics and Automation Letters. This is the author's version which has not been fully edited and content may change prior to final publication. Citation information: DOI 10.1109/LRA.2026.3688093

Design of an Active Haptic Interface using Proprioception Feedback for Continuous Endovascular Teleoperation

Ziyang Mei[1], Siyuan Han[2], Shengqian Qu[3], Ning Wang[3], Youchang Xia[3], Zitong Liao[3], Wenbo Zhou[3], Congxin Jie[3], Shuxiang Guo[4], Haizhen Wang[5], Yang Zhao[3], Gang Liu[2]

***Abstract*—Force feedback is essential for safe endovascular teleoperation, yet typically constrained by complex sensor integration. This paper presents a compact active haptic interface system designed for robotic catheterization. Leveraging the intrinsic proprioception of a Permanent Magnet Synchronous Motor, the integrated design enables proprioception proximal force measurement, simplifying mechanical structure while ensuring clinical deployability. To refine haptic fidelity, a hybrid estimation framework combines physics-based dynamics with a neural network to compensate for residual errors, optimizing the reconstruction of proximal interaction forces. The interface supports a continuous rate-control strategy, mapping estimated resistance into real-time active feedback. System experiments and user studies have demonstrated a delay of less than 5ms and a estimation accuracy of 0.1N. The proposed solution significantly reduces peak interaction forces and enhances obstacle awareness, offering a practical, cost-effective system-level solution for robotic vascular interventions.**

***Index Terms*—Vascular Interventional, Force Estimation, Field-oriented Control, Motor-based force feedback, Recurrent Neural Network**

I. INTRODUCTION

DURING conventional manual endovascular procedures, clinicians directly perceive variations in insertion resistance. However, in robot-assisted teleoperated interventions, the reconstruction of this haptic feedback remains a critical challenge [1], [2]. Addressing this challenge hinges on two components, the estimation of the interaction force and the rendering of this haptic feedback on the master manipulator.

Current force estimation strategies categorized into distal and proximal approaches. Distal methods attempt to directly measure the interaction forces between the interventional instrument and the tissue, whereas proximal methods measure the overall resistance encountered by the robotic mechanism while advancing the instrument. Distal force measurement relies on sensors at the instrument tip and is unaffected by multiple contributions along the insertion path. However, these sensorized instruments are not standard clinical tools, and their direct in vivo application faces unresolved clinical issues.

Proximal force measurement captures the resistance at the driving mechanism. Although it is affected by multiple contributions along the insertion path and cannot reflect isolated tissue forces, it corresponds to the feedback perceived by a clinician's hand during manual procedures. Therefore, using the proximal force as the source for haptic rendering is a reasonable approach. Consequently, many haptic feedback systems are built upon proximal force measurement architectures. Multiple studies highlight the growing demand for highly compact robotic systems in endovascular interventions [3]. While state-of-the-art platforms have demonstrated significant clinical efficacy, the structural integration of external force sensors presents substantial opportunities for footprint optimization.

Existing haptic interfaces for endovascular robots typically employ mechanisms such as magnetorheological (MR) brakes, magnetic powder brakes, or Series Elastic Actuators (SEAs). These configurations often involve specific fluid or powder containment, or utilize linear track mechanisms to render axial resistance. Alternatively, some works utilize motor control algorithms to directly generate haptic feedback. While this approach effectively simplifies the mechanical structure and enables compact designs, achieving high-fidelity haptic rendering remains a challenge to be addressed.

To bridge this gap, the contribution of this work is illustrated in Fig. 1. We first propose a direct wheel drive architecture without requiring external force sensors. Proximal force is estimated using the motor's proprioception and current measurements. A neural network is then applied to compensate for system nonlinearities, yielding the final force estimation. Additionally, the master haptic interface is directly driven by a motor, maintaining a simple and compact structure. This active configuration delivers continuous force feedback and is capable of maintaining torque generation even at zero angular

Manuscript received: December 15, 2025; Revised: March 9, 2026; Accepted: April 12, 2026. This paper was recommended for publication by Editor Pietro Valdastri upon evaluation of the Associate Editor and Reviewers' comments. This study was supported by the Major State Basic Research Development Program of China (2023YFB3810000, 2023YFB3810002 and 2023YFB3810003), the National Natural Science Foundation of China (8267073973, U24A20525 and U24A20746). Ziyang Mei and Siyuan Han contributed equally to this work. (Corresponding author: Shuxiang Guo, Haizhen Wang and Yang Zhao)

Ziyang Mei is with Institute of Artificial Intelligence, Xiamen University, Xiamen, 361005, China (e-mail: umeko@stu.xmu.edu.cn).

Siyuan Han and Gang Liu are with the School of Public Health and the Fujian Engineering Research Center of Molecular Theranostic Technology, Xiamen University, Xiamen, 361005, China (e-mail: hansiyuan@stu.xmu.edu.cn; gangliu.cmitm@xmu.edu.cn).

Shengqian Qu, Ning Wang, Youchang Xia, Zitong Liao, Wenbo Zhou, Congxin Jie and Yang Zhao are with Pen-Tung Sah Institute of Micro-Nano Science and Technology, Xiamen University, Xiamen, 361005, China (e-mail: qushengqian@stu.xmu.edu.cn; wangn@xmu.edu.cn; xiayc@stu.xmu.edu.cn; bruceliao@stu.xmu.edu.cn; zhouwenbo@stu.xmu.edu.cn; jiecongxin@stu.xmu.edu.cn; zhaoy@xmu.edu.cn).

Shuxiang Guo is with the Department of Electronic and Electrical Engineering, Southern University of Science and Technology, Shenzhen 518055, China, and also with the School of Life Science and the Key Laboratory of Convergence Medical Engineering System and Healthcare Technology, Ministry of Industry and Information Technology, Beijing Institute of Technology, Beijing 100081, China (e-mail: guo.shuxiang@sustech.edu.cn).

Haizhen Wang is with the Department of Anesthesiology, The First Affiliated Hospital of Xiamen University (Xiamen Anesthesia Quality Control Center), School of Medicine, Xiamen University, Xiamen, 361000, China (e-mail: 13959247925@163.com).

Digital Object Identifier (DOI): see top of this page.

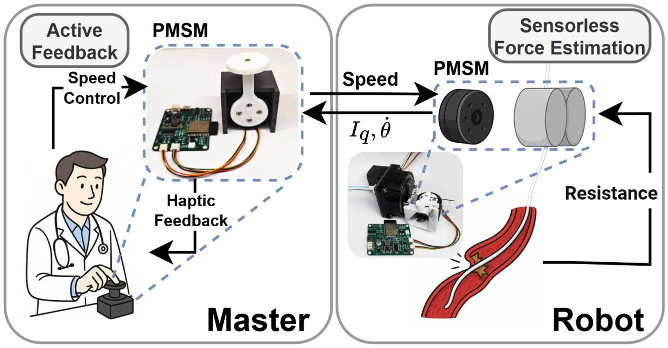

Fig. 1. Bilateral force and motion transfer between master console and robot.

velocity. Consequently, under a speed control paradigm, the operator can perceive dynamic force variations even while holding the joystick stationary to maintain a constant insertion speed. Finally, the proposed framework is validated through benchtop experiments and user studies. Experimental evaluations characterize the system's force estimation capability and active haptic rendering performance. Subsequent user studies demonstrate that the proprioceptive feedback reduces interaction forces during navigation, confirming the clinical viability of this compact architecture.

II. Related Works

A. Force Estimation in Vascular Robotics

Recent studies have explored various sensing modalities for force estimation in vascular robotics. For distal sensing, Lyu et al. [4] and Ren et al. [5] integrated micro-sensors directly at the instrument tip. Additionally, Jin et al. [6] proposed a vision-based approach to infer force from catheter deformation. This modality advantageously estimate localized tissue interaction, effectively isolating it from shaft friction. For proximal sensing, Du et al. [7] and Li et al. [8] integrated external load cells into the driving mechanism. Since this overall resistance replicates the manual tactile experience, proximal force serves as an ideal haptic source. However, integrating external load cells unavoidably increases the mechanical complexity and system footprint, whereas vision-based methods rely on sustained fluoroscopic exposure. Consequently, developing a structurally simplified and highly integrated force estimation method that accommodates standard clinical instruments without sustained X-ray exposure holds significant integration value.

B. Haptic Interfaces in Vascular Robotics

Recent haptic interfaces for endovascular robotics have explored various actuation mechanisms to enhance force fidelity and operational transparency. For semi-active and passive approaches, Guo et al. [9], Song et al. [10], and Duan et al. [11] developed interfaces using MR fluids or magnetic powder brakes, while Feng et al. [12] utilized magnetic repulsion. To introduce mechanical compliance, Wang et al., Shi et al. [13], and Yan et al. [14] proposed SEA-based systems incorporating spring elements. Additionally, Yan et al. [15] employ DC servo motors with synchronous belts to generate force feedback. Despite distinct actuation methods, these systems universally rely on linear architectures to replicate manual insertion and render axial feedback. While highly intuitive, the requisite linear tracks inevitably increase structural complexity and system footprint. Developing highly compact and streamlined haptic solutions is of immense value for clinical application and system integration.

C. Proprioception Force Estimation and Disturbance Rejection

Friction-wheel mechanisms enable continuous guidewire delivery [3], which improves task efficiency over clutch-based systems [16]. However, they introduce friction and noise that complicate actuator-current-based force estimation. Hardware-centric mitigation methods [17], [18] struggle to decouple internal friction from external forces. To bypass explicit physical modeling, data-driven algorithms [19], [20] have been utilized for friction compensation in general robotics. Consequently, establishing a data-driven framework to estimate insertion resistance via PMSM proprioception in endovascular interventions remains a critical objective.

III. Method

A. Robot Haptic Force Estimating

Recent research indicates that the human Just Noticeable Difference (JND) for force perception in endovascular tasks is approximately 0.192 N [11]. We utilize this value to design and evaluate the system, ensuring the resolution remain near this threshold to achieve optimal haptic feedback within the acceptable tolerance of user perception. To estimate the guidewire's inertial and resistive forces in real time, we propose a hybrid modeling framework combining physics-based dynamics with an Recurrent Neural Network (RNN) compensator and a Kalman filter for noise suppression [20]. The physical model captures the basic dynamics of the friction-wheel mechanism, while a lightweight Gate Recurrent Unit (GRU) network models unmodeled nonlinearities. The final state estimation of the inertial and contact forces is obtained through an Extended Kalman Filter (EKF) [21] that fuses model predictions and motor current measurements. The overall estimate method is shown at Fig. 2.

1) Physics-based Dynamics Model: The friction wheel drive system is first modeled as:

$$T_m = J_{eq}\ddot{\theta} + b\dot{\theta} + \tau_{friction} + rF_{physics} \quad (1)$$

where T_m is the motor torque estimated from the quadrature axis current I_q of the Field-Oriented Control (FOC) using the torque constant K_t as $T_m = K_t I_q$. J_{eq} is the equivalent inertia, b is the viscous damping coefficient, $\tau_{friction}$ models the non-linear Coulomb friction, r is the wheel radius, and $F_{physics}$ represents the proximal interaction force.

2) Dynamic Analysis of the Friction-Wheel System: To analyze the dynamic response characteristics of the friction-wheel mechanism used in our guidewire drive unit, we simulated its behavior under different equivalent inertias and

This article has been accepted for publication in IEEE Robotics and Automation Letters. This is the author's version which has not been fully edited and content may change prior to final publication. Citation information: DOI 10.1109/LRA.2026.3688093

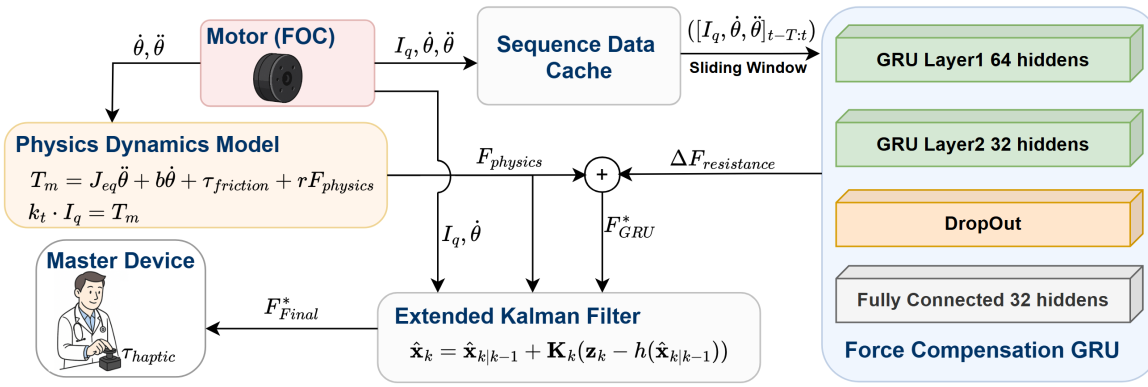

Fig. 2. The proposed force estimation architecture, comprising a physics-based model, a GRU residual compensator, and EKF post-processing for haptic feedback.

damping coefficients. The system is modeled by the second-order differential equation:

$$J_{eq}\ddot{\theta} + b\dot{\theta} + \tau_{friction} = T_m \tag{2}$$

where J_{eq} is the equivalent inertia of the rotating system (kg·m^2), b is the viscous damping coefficient (N·m·s/rad), $\tau_{friction}$ represents Coulomb friction torque (N·m), and T_m is the applied motor torque (N·m).

3) Recurrent based Nonlinear Compensation: Given the stringent real-time requirements of teleoperated haptic feedback, we employ a sequence-to-one GRU architecture. The network takes as input a sliding window of the most recent T sensor readings $[I_q, \dot{\theta}, \ddot{\theta}]_{t-T:t}$, where T is to capture temporal dependencies. This design allows the GRU to implicitly encode the system dynamics within its hidden states and output a corrected resistance force estimate at each time step without requiring explicit propagation of hidden states across inference steps.

The network predicts the nonlinear residual component of the resistance force:

$$\Delta F_{resistance} = f_{GRU}\left([I_q, \dot{\theta}, \ddot{\theta}]_{t-T:t}\right) \tag{3}$$

where $f_{GRU}(\cdot)$ denotes the recurrent network mapping.

The corrected insertion force is then expressed as:

$$F^*_{GRU} = F_{physics} + \Delta F_{resistance} \tag{4}$$

where $F_{physics}$ is obtained from the physics-based friction-wheel dynamics model. This sequence-to-one GRU framework achieves low-latency inference suitable for real-time haptic feedback while benefiting from improved robustness against measurement noise and unmodeled nonlinearities.

The GRU network in our framework is not designed to directly predict the total insertion force $F_{physics}$ from scratch. Instead, it serves as a residual compensator that models the unmodeled nonlinearities and disturbances of the physics-based model. This hybrid design provides several advantages: (1) the physics-based model encapsulates known system dynamics and constraints, ensuring reasonable baseline predictions even in unseen scenarios. (2) The GRU network focuses only on learning the complex residual components $\Delta F_{resistance}$, such as friction hysteresis, stick-slip, and guidewire bending effects, reducing its complexity and data requirements. (3) This separation of responsibilities improves interpretability and allows the model to leverage domain knowledge for better generalization. By combining structured physical priors with data-driven residual learning, the system achieves both high fidelity and robustness in real-time force estimation.

4) State Estimation via EKF: To enhance robustness against measurement noise and improve the reliability of force estimation, we employ an EKF [21]. The system state vector is defined as $\mathbf{x} = \begin{bmatrix} F_{physics} \\ F^*_{GRU} \end{bmatrix}$ and the measurement vector is $\mathbf{z} = \begin{bmatrix} I_q \\ \dot{\theta} \end{bmatrix}$. $F_{physics}$ represents the estimated inertial contribution from the guidewire drive system, and F^*_{GRU} is the corrected proximal insertion force predicted by the physics-GRU hybrid model. Although these forces are not directly measurable, they influence the observable motor quantities I_q and $\dot{\theta}$ through the system dynamics, this relationship enables the EKF to infer the hidden states by predicting expected measurements $\hat{\mathbf{z}}_k = h(\hat{\mathbf{x}}_{k|k-1})$ and comparing them against the actual noisy measurements $\mathbf{y}_k = \mathbf{z}_k - \hat{\mathbf{z}}_k$, where $\mathbf{y}_k$ is the residual. The Kalman gain $\mathbf{K}_k$ adjusts this residual to update the state estimate $\hat{\mathbf{x}}_k = \hat{\mathbf{x}}_{k|k-1} + \mathbf{K}_k\mathbf{y}_k$, effectively blending model predictions with measurement information.

The $\mathbf{z}$ contains only directly measurable quantities from the motor sensors, while the latent force components $[F_{resistance}, F^*_{GRU}]$ are indirectly inferred. The EKF serves as a fusion layer that compensates for modeling inaccuracies and sensor noise, producing a refined proximal insertion force estimate F^*_{Final}, which is subsequently rendered to the master device for haptic feedback.

B. Master Device Haptic Feedback and Speed Control

The master device, illustrated in Fig. 3, is a rotary dial actuated by a PMSM. It serves as both a teleoperation input and a haptic display, featuring auto-centering dynamics based on a virtual spring-damper. The operator controls the guidewire's insertion velocity v_{gw} by adjusting the rotation angle θ_m as defined by:

$$v_{gw} = k_v \cdot \theta_m \tag{5}$$

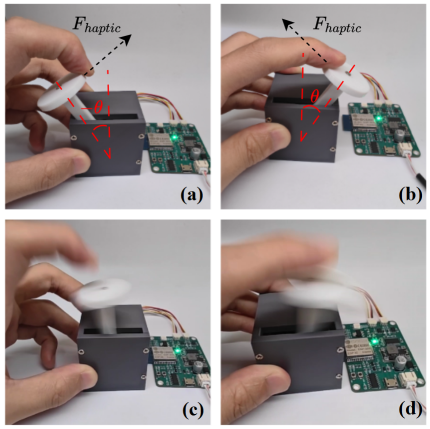

Fig. 3. The haptic master device. (a) and (b) illustrate the operator rotating the dial to set a desired guidewire speed, while simultaneously experiencing a haptic feedback torque F_{haptic} opposing rotation angle θ. (c) and (d) illustrate the dial automatically returning to its neutral position after release, enabled by a virtual spring-damper.

where k_v is a user-defined scaling factor (m/s/rad). This mapping enables intuitive guidewire manipulation: clockwise dial rotation advances the guidewire, and counterclockwise rotation retracts it.

Simultaneously, the dial renders haptic feedback reflecting interaction forces from the follower robot. The dynamic behavior of the dial is described by:

$$J_m\ddot{\theta}_m + B_m\dot{\theta}_m + \tau_{friction} = \tau_{motor} + \tau_{haptic} \tag{6}$$

where J_m is the moment of inertia of the dial (kg·m^2), B_m is the viscous damping coefficient (Nms/rad), $\tau_{friction}$ represents the static and Coulomb friction torque, τ_{motor} is the control torque generated by the PMSM, and τ_{haptic} is the haptic torque rendered based on the interaction forces estimated at the follower side.

1) Haptic Torque Computation: The proximal insertion force $F_{insertion}$ estimated at the follower side is mapped to a haptic torque:

$$\tau_{haptic} = G_h \cdot F_{insertion} \tag{7}$$

where G_h is a gain factor. To enhance stability and user comfort, deadband filtering and saturation are applied.

2) Virtual Spring-Damper Modeling: To support return-to-neutral behavior when the dial is released, a virtual spring-damper model is applied:

$$\tau_{return} = -K_s(\theta_m - \theta_{ref}) - B_s\dot{\theta}_m \tag{8}$$

This prevents unintended guidewire movement and provides a self-centering effect.

3) Torque-Current Mapping and FOC Control: The total desired torque is derived as:

$$\tau_{total} = \tau_{haptic} + \tau_{return} \tag{9}$$

Standard PMSM control assumes a constant torque coefficient K_t. However, our calibration experiments demonstrated hysteresis behavior, yielding distinct curves for increasing and decreasing torque output.

To compensate for this, an experimental inverse mapping function Ψ is constructed using high-order polynomial fitting. The command current is generated as:

$$i_{q,cmd} = \Psi(\tau_{total}, \text{sgn}(\dot{\tau}_{total})) \tag{10}$$

where Ψ selects the appropriate fitted coefficients based on the rate of change of torque $\dot{\tau}_{total}$ to address the hysteresis effect. This ensures precise haptic transparency consistent with the measured motor characteristics.

IV. Experiments and Results

A. Hardware and Control Architecture

The experimental evaluation was conducted using a custom-built telerobotic system. The low-level motor control is executed by distributed ESP32 microcontrollers. Each control unit drives a 2804 gimbal PMSM using a DRV8313 motor driver, while an INA240 current sense amplifier and an AS5600 magnetic rotary encoder are integrated to provide precise current and position feedback. Two such modular units are employed in the system to independently actuate the guidewire propulsion mechanism and the haptic feedback interface. To enable guidewire rotation, the PMSM-based delivery mechanism is integrated into a hollow rotary platform.

The system implements a master-slave teleoperation architecture facilitated by two separate host computers. The follower-side guidewire robot is controlled by a Raspberry Pi 4B, which handles hardware interfacing and data aggregation. Conversely, the master manipulator is connected to a high-performance laptop equipped with an NVIDIA RTX 2060 GPU. This laptop hosts the high-level computational tasks, specifically running the GRU network and EKF algorithms for force estimation and haptic rendering. Communication between the motor drive modules and the host computers is established via high-speed serial ports, while the master and slave computers exchange data through a low-latency Ethernet connection. The system achieves a hardware data acquisition rate of 100 Hz; however, the algorithmic processing pipeline operates at 50 Hz to ensure robustness against network jitter and to maintain a stable, non-oscillatory haptic feedback loop.

B. Master Follower Velocity Tracking

To rigorously evaluate the fidelity of the proposed proprioceptive velocity estimation, we established a ground truth validation platform, As illustrated in Fig. 4 (a). The PMSM shaft was physically coupled to a high-precision incremental rotary encoder (Model E6B2-CWZ6C, 2000 P/R), The encoder's quadrature output signals were captured using the hardware Pulse Counter (PCNT) peripheral of the ESP32 microcontroller.

The angular velocity measured by the external encoder was compared against the expected velocity command Expected $\dot{\theta}$. As illustrated in Fig. 4(b)-(c), the measured response closely tracks the target trajectory, accurately capturing the dynamic characteristics including the transient rise under ramp excitation and rapid stabilization following step inputs. This validates the high fidelity of the proposed velocity control

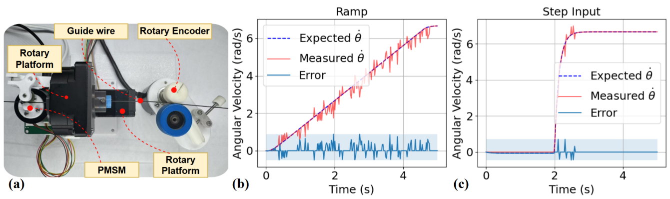

Fig. 4. Velocity tracking validation. (a) The ground truth experimental setup featuring a PMSM coupled with a high-precision incremental encoder. (b)-(c) Comparison between expected and measured angular velocity $\dot{\theta}$ under different inputs, demonstrating dynamic tracking performance.

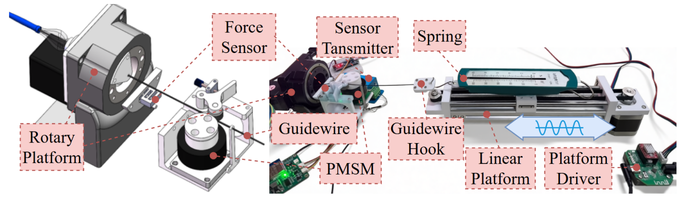

Fig. 5. Experimental platform for guidewire force estimation, including the PMSM module, force sensor, guidewire hook, spring, and linear platform.

TABLE I
QUANTITATIVE TRACKING PERFORMANCE UNDER RAMP AND STEP INPUT CONDITIONS.

Metric	Ramp Input	Step Input
MAE (rad/s)	0.1232	0.0382
RMSE (rad/s)	0.2441	0.0929
Max Error (rad/s)	0.8800	0.7000
Steady-State Error (rad/s)	-	<0.001
Tracking Score (%)	96.34	98.62

TABLE II
ERROR METRICS OF FORCE ESTIMATION AT DIFFERENT EXCITATION FREQUENCIES.

Frequency (Hz)	RMSE (N)	MAE (N)	MaxAE (N)
0.5	0.0669	0.0535	0.2760
1.0	0.0828	0.0675	0.2429
1.5	0.1050	0.0828	0.3588
2.0	0.0678	0.0549	0.1920
2.5	0.1052	0.0857	0.3503
3.0	0.0971	0.0833	0.2465

scheme, confirming that the actuation system provides the precise motion transmission required for surgical interventions.

To quantitatively evaluate the velocity tracking performance of our scheme, Table I reports the error metrics, specifically Mean Absolute Error (MAE) and Root Mean Square Error (RMSE) for the ramp and step input conditions. Across both excitation patterns, the physics-based model demonstrates low tracking error, with RMSE values below 0.25 rad/s for the ramp input and below 0.10 rad/s for the step input. To provide a normalized measure of tracking quality, we compute an RMSE based tracking score defined as:

$$\text{Tracking Score} = \left(1 - \frac{\text{RMSE}}{\Delta\omega}\right) \times 100\% \tag{11}$$

where $\Delta\omega = \max(\omega) - \min(\omega)$ denotes the dynamic range of the expected angular velocity. As shown in Table I, the proposed model achieves tracking scores of 96.34% for the ramp input and 98.62% for the step input, confirming its high fidelity in both dynamic and steady-state regimes. the system demonstrates a low end-to-end velocity response latency of less than 5 ms.

C. Force Estimation

A dynamic characterization platform was designed to calibrate the force estimation model as shown in Fig. 5. In this scenario, the guidewire motor remains stationary while a linear motion module applies controllable sinusoidal loads to the guidewire tip via an elastic coupling, converts the prescribed displacement into a controllable force input. A force sensor (DYLY-109, DAYSENSOR) is installed between the motor framework and the fixed platform to record the ground truth proximal interaction forces.

Across the tested excitation frequencies,the error metrics is shown at Table II, indicate that the force estimation remains generally stable and accurate. At lower frequencies, the reconstruction shows consistently small deviations from the sensor output, reflecting a reliable quasi-static relationship. As frequency increases, the errors exhibit only a mild upward tendency rather than a sharp deterioration, suggesting that the estimator retains robustness within the investigated bandwidth, as shown in Fig. 6. These results show that under the force-estimation condition with zero angular velocity, the PMSM estimator achieves high accuracy and consistent performance across frequencies, making it a reliable baseline for subsequent dynamic modeling and GRU-based compensation.

The experimental setup, shown in Fig. 7, is designed to validate the force estimation capabilities of the physics-based model and to collect data for training and testing the nonlinear compensation models. It consists of the interventional robot, force sensors, and a vascular phantom for guidewire manipulation. The distal force sensor mounted on the vascular phantom is used to monitor the interaction forces for safety evaluation during manipulation, while the force sensor installed between PMSM module and robot frame provides the reference force signal that the estimator aims to reproduce. Guidewire motions are executed through a PTFE tube into the vascular phantom, and the resulting insertion forces are recorded to train and evaluate the PMSM estimator and its nonlinear compensation under realistic operating conditions.

To train the GRU compensator, a dataset using the full guidewire insertion system under various teleoperation scenarios was collected. The input features include a sliding window of recent measurements: motor current I_q, angular velocity $\dot{\theta}$, and angular acceleration $\ddot{\theta}$. The ground truth proximal insertion force F_{ref} was measured using the sensor installed between motor framework and the fixed base.

The network was trained to minimize the residual error:

$$\mathcal{L} = \frac{1}{N}\sum_{t=1}^{N}\left(f_{\text{GRU}}([I_q, \dot{\theta}, \ddot{\theta}]_{t-T:t}) - r_t\right)^2 \tag{12}$$

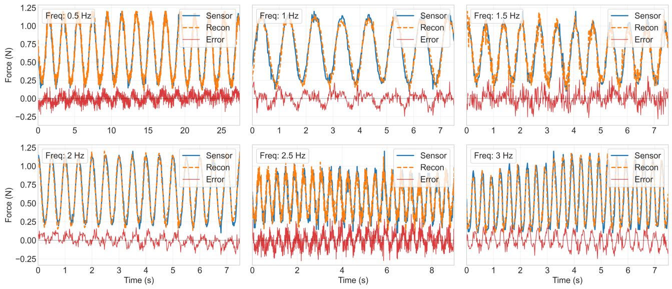

Fig. 6. Force estimation results at excitation frequencies ranging from 0.5 Hz to 3 Hz, showing the PMSM-reconstructed force, sensor-measured force, and the corresponding estimation error.

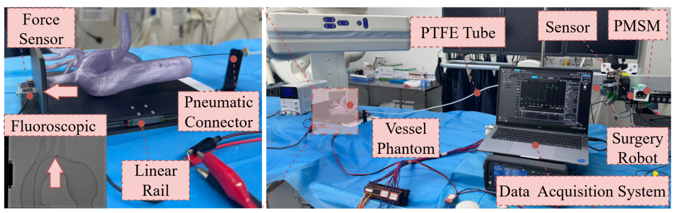

Fig. 7. Experimental setup for force estimation. Collecting insertion forces for the training and evaluation of our methods.

where:

$$r_t = F_{\mathrm{ref},t} - F_{\mathrm{physics},t} \tag{13}$$

$F_{physics}$ is the output of the analytical dynamics model. The training dataset was collected using the experimental platform shown in Fig. 7, where motor current, angular velocity, and the proximal DYLY-109 sensor readings were recorded. Each training sample corresponds to a sliding time window of T timesteps, and input features were normalized to zero mean and unit variance. The dataset contains 150 sequences with $60,000$ samples, which was randomly split into 80% for training and 20% for validation. The GRU was implemented in PyTorch and trained using the Adam optimizer with learning rate = 1×10^{-4} and batch size = 32 for 100 epochs. The best model was selected based on RMSE.

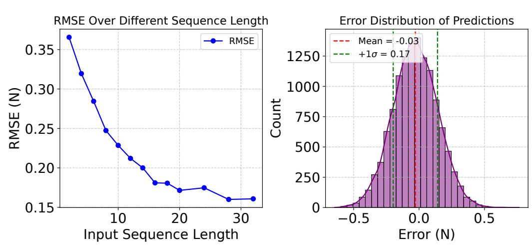

Fig. 8. Performance evaluation over different input sequence length and error distribution of GRU predictions.

The performance of the GRU model was evaluated in Fig. 8. By analyzing the relationship between the input sliding time window length T with the RMSE, as well as by examining the residual distribution of the model's predictions. The curve indicates a clear decrease in RMSE as the sequence increases, and RMSE stabilizing after sequence length of 20. This suggests that a longer sequence enables the model to better capture temporal dependencies. The residual distribution of the GRU model's predictions at T=20 is also shown, this reveals that the prediction errors are tightly clustered around zero, with minimal systematic bias and low variance, suggesting high estimation accuracy and consistency.

TABLE III
COMPARISON OF DIRECT FORCE PREDICTION AND RESIDUAL PREDICTION COMBINED PHYSICS MODEL

Method	RMSE	Mean Error	Std
Residual Prediction + F_{model}	0.171	-0.028	0.169
Direct Prediction of F	0.358	0.077	0.350

To further evaluate the effectiveness of the hybrid modeling approach, we compare the force estimation performance of a direct end-to-end prediction model against the proposed physics-guided residual learning method in Table III. The results show that the residual prediction method, which corrects the physics-based model output with a GRU-based compensator, achieves a lower RMSE, reduced mean error, and smaller standard deviation. This demonstrates that incorporating physical priors improves both the accuracy and robustness of the force estimation, validating the effectiveness of the proposed framework. To improve the temporal consistency of the estimated proximal force, an EKF was deployed as a post-processing step using the FilterPy library [22]. In this implementation, the Kalman gain is determined by the process noise covariance Q and measurement noise covariance R. These matrices were established utilizing the sampled offline dataset. Specifically, R was quantitatively determined by calculating the variance of the force sensor readings under static conditions. Meanwhile, Q was heuristically optimized by progressively increasing its value to minimize tracking delay, and the tuning was capped at the threshold where mechanical noise and network jitter began to induce perceivable oscillations in the haptic feedback loop. The tuned EKF was then applied to the hybrid force estimates, as shown in Fig. 9.

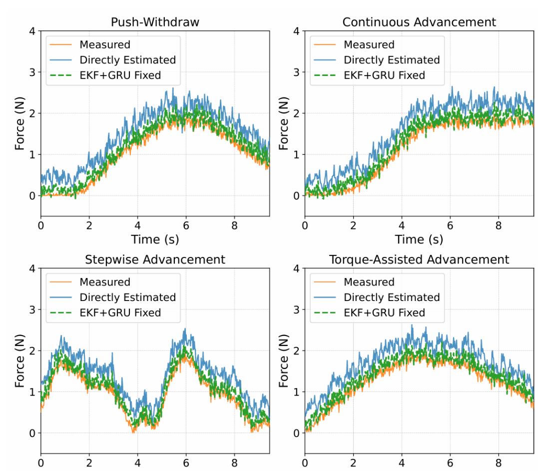

Fig. 9. Estimated force under four representative cases. Compared with the measured force, the nonlinear correction effectively reduces the estimation error and aligns better with actual observations.

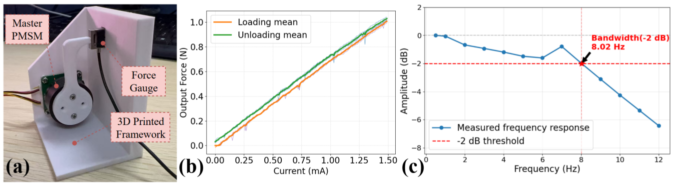

Fig. 10. Characterization of the master haptic controller. (a) Experimental setup. (b) Relationship between current and output force. (c) Frequency response and -2 dB bandwidth.

D. Haptic Feedback Experiments

To characterize the haptic unit, we built a benchtop setup where the master PMSM drives a lever that presses against a force gauge, as shown in Fig. 10 The resulting current to force data are plotted in Fig. 10 (b). The current–force characteristics are approximated by second-order polynomials as

$$F_{\text{load}}(i) = -0.023155\, i^2 + 0.725796\, i - 0.019272 \quad (14)$$

$$F_{\text{unload}}(i) = -0.043098\, i^2 + 0.743892\, i + 0.022228 \quad (15)$$

where i denotes the motor current (mA) and F is the output force (N). The loading fit $F_{\text{load}}(i)$ and unloading fit $F_{\text{unload}}(i)$ exhibit a nearly linear trend with a small hysteresis loop, which is acceptable for our application. In the following experiments, the unloading polynomial is used to map the commanded motor current to the expected haptic force rendered at the master side.

After the master PMSM calibrated, we evaluated the dynamic response of the haptic output unit. The motor was driven by sinusoidal current commands with frequencies ranging from 1 Hz to 12 Hz, and the resulting contact force was measured by the force gauge at the end-effector. The current amplitude was chosen such that the nominal force remained within the comfortable interaction range for the user.

Fig. 11 shows the measured time-domain force responses for representative excitation frequencies from 1 Hz to 12 Hz. At low frequencies (up to approximately 4–5 Hz), the rendered force follows the sinusoidal reference closely, with nearly constant amplitude and negligible distortion. As the frequency increases, a gradual attenuation of the force amplitude can be observed, together with a slightly increased cycle-to-cycle variability, which reflects the finite bandwidth of the haptic actuation and control loop. Across to Fig. 10 (c), The gain remains within about -2 dB up to roughly 8 Hz, beyond which the amplitude decays more rapidly. This suggests that the effective haptic bandwidth of the master side is on the order of 8 Hz, Meanwhile, under wired connection, the measured end-to-end force latency of the system less than 5 ms. which is sufficient to reproduce the dominant components of the interaction forces encountered in interventional surgery procedures.

We conducted a user study with 36 participants stratified into three experience groups: 20 engineering outsiders, 8 novice doctors, and 8 expert interventional physicians. The experimental platform is same in Fig. 7 mentioned before. Participants operated a dual-joystick interface: a standard joystick controlled the rotational speed of the guidewire,

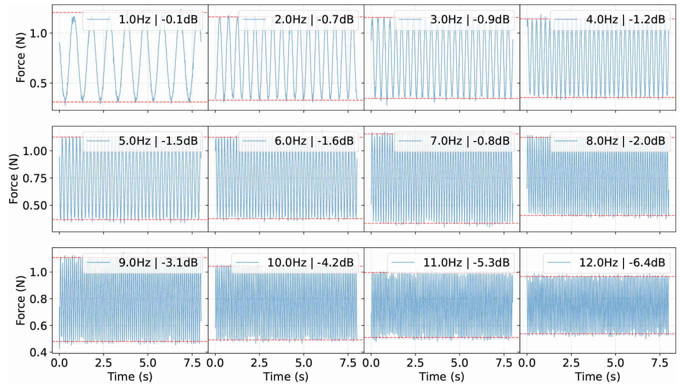

Fig. 11. Time-domain force responses from 1 to 12 Hz of the master haptic device.

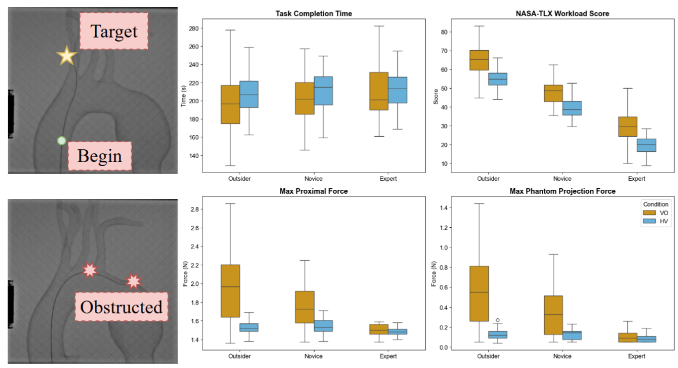

Fig. 12. Task performance across experience levels under two control modes.

while the custom haptic master device controlled the delivery speed. They were tasked with navigating the into the left common carotid artery (LCCA). During this procedure, contact between the guidewire and the phantom is inevitable, as the guidewire frequently slide into the target branch while maintaining contact with the wall. Participants were instructed to minimize the contact force between the instrument and the phantom while completing the navigation task as efficiently as possible. Participant performed the navigation task under two conditions: a Visual-Only (VO) mode relying solely on visual feedback, and a Haptic-Visual (HV) mode that supplemented the visual feed with synchronized haptic force reflection from the robot.

The results in Fig. 12 demonstrate the safety and efficacy of the proposed proprioceptive framework. While task completion times were comparable between modes, the slightly increased durations under the haptic mode indicate a more deliberate navigation strategy. This aligns with recent human-factors research demonstrating that haptic feedback prompts operators to move more cautiously, which inherently lowers the contact forces exerted on tissues [23]. Crucially, the active haptic mode effectively constrained the peak interaction forces; both the maximum proximal force and the maximum phantom projection force were substantially reduced across all experience levels. In addition to the visual cues of device deformation [2], the system provides supplementary tactile feedback. This augmented sensory information offers greater reference value for operators, enabling them to better reduce interaction forces and maintain instrument-tissue interactions within strictly safer limits. Furthermore, the significantly lower NASA-TLX scores indicate a more comfortable user experience. This is consistent with recent findings that haptic feedback effectively alleviates the sustained concentration required for visual force compensation, thereby reducing overall operator fatigue [23].

V. Conclusions

This paper presents a compact, integrated active haptic interface designed to restore tactile perception in robotic endovascular teleoperation. By employing a data-driven framework, we effectively estimated proximal interaction forces from noisy motor currents, providing an active force feedback scheme for continuous speed control. User studies demonstrate that this active feedback provides intuitive tactile cues, enabling operators to perceive relative resistance changes. Consequently, it significantly reduces peak interaction forces, while subjective evaluations confirm that it provides a more comfortable and effortless operating experience. However, limitations exist: torsional resistance remains unreconstructed, validation is restricted to phantoms, and the trained GRU model is currently limited to specific hardware and instrument specifications. Future work will involve animal trials to evaluate surgical efficacy, and integrate transfer learning to dynamically adapt the data-driven model to different instruments and setups without extensive retraining.

References

[1] G. Najafi, K. Kreiser, M. E. Abdelaziz, and M. S. Hamady, "Current state of robotics in interventional radiology," *CARDIOVASC INTER RAD*, vol. 46, no. 5, pp. 549–561, 2023.

[2] G. Gravino, "Haptic feedback in robotic endovascular neurosurgical intervention: A necessity or a commodity?," 2025.

[3] N. T. Kantu, W. Gao, N. Srinivasan, G. D. Buckner, and H. Su, "Portable and versatile catheter robot for image-guided cardiovascular interventions," *IEEE/ASME Trans. Mechatron.*, vol. 30, no. 6, pp. 7985–7994, 2025.

[4] C. Lyu, S. Guo, Y. Yan, Y. Zhang, Y. Zhang, P. Yang, *et al.*, "Deep-learning-based force sensing method for a flexible endovascular surgery robot," *IEEE Trans. Instrum. Meas.*, vol. 73, pp. 1–10, 2024.

[5] B. Ren, Y. Zhao, J. Zhang, C. Wang, H. Li, and J. Zhang, "Multi-point bending operation force detection method of catheter-based on rotary clamping delivery," *Sens. Actuators A: Phys.*, vol. 382, p. 116128, 2025.

[6] R. Jin, J. Chen, P. Hu, and J. Li, "Optimizing sensorless control in pmsm based on the sogifo-x flux observer algorithm," *Sensors*, vol. 24, no. 3, p. 817, 2024.

[7] W. Du, G. Yi, O. M. Omisore, W. Duan, T. O. Akinyemi, X. Chen, *et al.*, "Analyzing surgeon–robot cooperative performance in robot-assisted intravascular catheterization," *IEEE Trans. Hum.-Mach. Syst.*, 2024.

[8] X. Li, S. Guo, P. Shi, X. Jin, and M. Kawanishi, "An endovascular catheterization robotic system using collaborative operation with magnetically controlled haptic force feedback," *Micromachines*, vol. 13, no. 4, p. 505, 2022.

[9] S. Guo, Y. Song, X. Yin, L. Zhang, T. Tamiya, H. Hirata, *et al.*, "A novel robot-assisted endovascular catheterization system with haptic force feedback," *IEEE Trans. Robot.*, vol. 35, no. 3, pp. 685–696, 2019.

[10] Y. Song, Y. Tian, L. Li, Q. Gao, and Z. Li, "Passive haptic interface for robot-assisted endovascular catheterization," *Med. Biol. Eng. Comput.*, vol. 63, no. 10, pp. 3067–3082, 2025.

[11] W. Duan, Z. Li, O. M. Omisore, W. Du, T. O. Akinyemi, X. Chen, *et al.*, "Development of an intuitive interface with haptic enhancement for robot-assisted endovascular intervention," *IEEE Trans. Haptics*, vol. 18, no. 1, pp. 80–92, 2023.

[12] Y.-Z. Feng, S.-Q. Liu, X.-L. Xie, X.-H. Zhou, J.-X. Wang, C.-C. Fan, *et al.*, "A novel haptic interface for enhancing operational transparency in robot-assisted vascular interventional surgery," *IEEE Trans. Med. Robot. Bionics*, 2025.

[13] P. Shi, S. Guo, L. Zhang, X. Jin, H. Hirata, T. Tamiya, *et al.*, "Design and evaluation of a haptic robot-assisted catheter operating system with collision protection function," *IEEE Sens. J.*, vol. 21, no. 18, pp. 20807–20816, 2021.

[14] Y. Yan, S. Guo, C. Lyu, J. Guo, J. Wang, P. Yang, *et al.*, "A novel sea-based haptic interface for robot-assisted vascular interventional surgery," in *Proc. IEEE Int. Conf. Robot. Autom.*, pp. 5871–5876, 2024.

[15] Y. Yan, H. Wang, H. Yu, F. Wang, J. Fang, J. Niu, *et al.*, "Machine learning-based surgical state perception and collaborative control for a vascular interventional robot," *IEEE Sens. J.*, vol. 22, no. 7, pp. 7106–7118, 2022.

[16] R. Baozhen, Z. Yan, Z. Jianhua, and Z. Jianjun, "Catheter friction drive based on rotary clamp delivery," *J. Mech. Eng.*, vol. 60, no. 17, pp. 80–90, 2024.

[17] P. Li, J. Feng, X. Zhang, D. Fang, J. Zhang, and C. Liang, "Modeling and experimental study of the intervention forces between the guidewire and blood vessels," *Med. Eng. Phys.*, vol. 127, p. 104166, 2024.

[18] A. A. Nazari, J. Catania, S. Sadeghian, A. Jalali, H. Masnavi, F. Janabi-Sharifi, *et al.*, "A master-follower teleoperation system for robotic catheterisation: Design, characterisation and tracking control," *Int. J. Med. Robot. Comput. Assist. Surg.*, vol. 21, no. 3, p. e70073, 2025.

[19] F. Cao, P. D. Docherty, S. Ni, and X. Chen, "Contact force and torque sensing for serial manipulator based on an adaptive kalman filter with variable time period," *Robot. Comput.-Integr. Manuf.*, vol. 72, p. 102210, 2021.

[20] S. Liu, L. Wang, and X. V. Wang, "Sensorless force estimation for industrial robots using disturbance observer and neural learning of friction approximation," *Robot. Comput.-Integr. Manuf.*, vol. 71, p. 102168, 2021.

[21] D.-J. Jwo and T.-S. Cho, "Critical remarks on the linearised and extended kalman filters with geodetic navigation examples," *Measurement*, vol. 43, no. 9, pp. 1077–1089, 2010.

[22] R. Roger and J. Labbe, "Filterpy - kalman filters and other optimal and non-optimal estimation filters in python." https://github.com/rlabbe/filterpy, 2025. Accessed: 2025-07-26.

[23] E. D. Gomez, H. M. Husin, K. R. Dumon, N. N. Williams, and K. J. Kuchenbecker, "Simulation training with haptic feedback of instrument vibrations reduces resident workload during live robot-assisted sleeve gastrectomy," *Surg. Endosc.*, vol. 39, no. 3, pp. 1523–1535, 2025.